Electrodes-oxide-semiconductor device for biosensing: ☆ renewed conformal analysis and multilayer algorithm

Rémi S. Pampin*, Jean-Pierre Raskin, Isabelle Huynen, Denis Flandre

ICTEAM Institute, ELEN Division, Place du Levant 3, B-1348 Louvain-la-Neuve, Belgium

Abstract

Intelligence technologies aim at providing sense organs to machines such as artificial nose or tongue. Inspired by chemically-sensitive devices and antenna couplers, the Insulated Substrate Impedance Transducer (ISIT) reacts to neighboring electro-active targets by changes in its built-in properties, measured through interface electrodes. Exhaustive comprehension of their interactions with medium and substrate is key to ISIT operation and embodiments efficiency. Among simulation approaches, versatile numerical methods, handy conformal analyses and other partial capacitances yet require computational tuning while loosely ensuring previsions quality. The present work then revisits compact modeling of the ideal though essential 2D cases, planar interdigitated electrodes lengthy-fingers arrays on various materials stacks. Starting from a passive membrane with or without back contact, it tackles computability at thin-film and infinite-medium horizons given clear definitions. Optimally simplified formula are proven for membrane thickness down to zero and fingers' spacing around 10 % to 90 % of their periodicity. A straightforward algorithm going beyond "partial-images" is further proposed for multilayers. Sounded for engineers, it is generic, fast and accurate up to 4 arbitrary substrate layers. The method is verified against extensive Finite Elements and validated with measurements in a metallic biolabels sensing application.

Keywords: Interdigitated array, coplanar coupler, strip-line, partial-capacitance, modeling, field effect

1. Introduction

Surface coupled electrodes can be found in semiconductors devices [2–4], electromechanical energy harvesters or millimeter-waves couplers [5–7], low-

☆ISIT stands for "Insulated Substrate Impedance Transducer(s)", IDA for 'InterDigitated Array'.

*Corresponding author

Email addresses: remi.pampin@net-c.com (Rémi S. Pampin), denis.flandre@uclouvain.be (Denis Flandre)

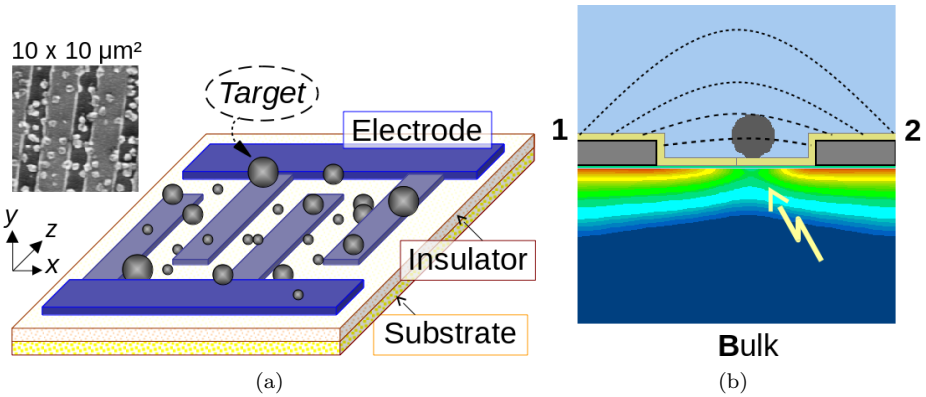

Figure 1: Insulated Substrate Impedance Transducers [1]; (a) planar electrodes IDA for sensing target analytes – here metallic biolabeling particles – imaged at the top by Scanning Electron Microscopy; (b) electrodes fingers pair and interdigital gap on bulk semiconductor, denoting connections, inner potential and external coupling lines.

frequency sensors [8–10] or actuators [11–13], and radio-amplifiers [14–16]. Modeling of coplanar and microstrip waveguides or filters above 10 MHz attracted attention for half a century [7, 17–19], whereas integrated and hybrid electronics have brought interest to the quasistatic regime for characterization or physico-chemical transduction [3, 20, 21]. In spite of their diversity, embodiments like interdigitated combs, spiral inductors, meanders and combinations of them [22–24] share similar physical and mathematical considerations for describing the fields across conductors. This publication focuses on periodic arrays formed by a pair of interleaved identical electrodes deposited on planar substrates. Frequent wonders concern miscellaneous layers influence nearby devices surface [2, 25–27]. For the Insulated Substrate Impedance Transducer (ISIT [1, 28]) depicted in Figure 1, materials of various properties and thicknesses are piled-up below surface micro-electrodes. Beyond simple interdigitated arrays (IDA) where support is considered passive, ISIT uses an active substrate whose electric charge carriers interact with close detection targets. While developed as innovative semiconductor-based biosensors [28–30], verified analytical algorithms were still lacking for proving how the transducer works and paving the way to its sub-parts specific de-embedding. Modeling such non-linear building blocks is error-prone, as for open-gate transistors or coplanar waveguides, and multistage approximations undermine mastery of the whole [31]. On the contrary, good analytical models implemented as parametric modules in higher-level Computer-Aided Design tools, like device or circuit simulators [32, 33], help following wider design flows. But computation speed and cumulative precision are critical.

Most versatile simulation methods proceed through electric or magnetic fields evaluation, by fitting particular functions into finite meshes over physical domains. They rely on finite elements [34–36], numerical series decomposition in geometric or Fourier space [21, 37–39], or combined approaches known as variational, integral or relaxation equations [40, 41]. Materials anisotropy can

be handled *via* spectral decomposition [42, 43]. Nevertheless, several drawbacks shall be reminded. First, setup details like sampling resolution and solver tolerance silently condition results quality. In other words, basis functions and iterations numbers have impacts on convergence speed and residual errors. Without a global objective criterion, choosing a trade-off there turns down to trial-and-errors cycles under expert judgment. Loose timing or geometrical constraints – released by quasi-static small-signal hypotheses typically – don't even help. Second, internal potentials computation increases overheads when only global conductance or effective properties mater. Lastly, simulated devices remain black boxes to the designer since structure-related lumped-element model can barely be identified.

As an alternative, conformal analysis leads to inter-electrodes characteristics close-form expressions. But their steep learning curve, questionable scope and software implementation pitfalls compromise their widespread. Computation of elliptic functions and integrals [44, 45] also degrades intuitiveness. Subtleties between resembling formulas turn out difficult to distinguish for interdigital mono-, bi- or poly-gaps (arrays of respectively two, three, or more fingers [46, 47]) and coplanar waveguides with lateral infinite ground planes – or narrow gap. Literary profusion dedicated to applicative outcomes further tends to evade theoretical bases yet essential to clarify notations, validate tests and push robust developments further [31]. State-of-the-art works have reconsidered computability and applicability issues [31, 48]; but balancing accessibility, accuracy and completeness stays challenging. More special cases tend to be treated apart as exactness requirements sharpen, but at concision expense. IDA electrodes, called poly-gap for their fingers multiplicity, are finally reported here but not the single-gap, two-lines pair. The latter indeed follows hyperbolic transformations well covered by literature while the former presents an incomplete elliptic integral in the path – more difficult to handle.

Next, multilayer substrate devices with complex capacitance or admittance spectra call for conformal analysis integration into larger algorithms. Convenient *partial capacitances* (P.C.) and underlying *effective permittivity* assumptions have been regularly revisited, but without much enlarging the consensus about their justification so far [31, 48, 49]. Terms of "permittivity" and "capacitance" are here commonly understood as complex quantities, for including conductive parts or ohmic losses. Authors as Ghione, Gevorgian, Dias & Igreja involved P.C. frameworks to take the interface into account at the backside of thin microstrips supporting planar lines pairs [49–52]. Sytchev, Dias & Igreja further described poly-gap IDA in contact with outwards monotonically decreasing or increasing permittivity layers [50, 53]. Marginal approximations at limit-case shape ratios improve software portability, but design corners and computation thresholds are never fully covered (e.g. at thin film or small gap). Recently, modified- P.C. and recursive images were proposed to handle non-monotonic permittivities stacks [48, 54]. But the latter has computation overheads for capacitance evaluation, while the former iterates layers in a wrong way to fully take distant interfaces cross-talks into account. Both nevertheless will be discussed against some of our results. Keeping effective or *partial* permittivities

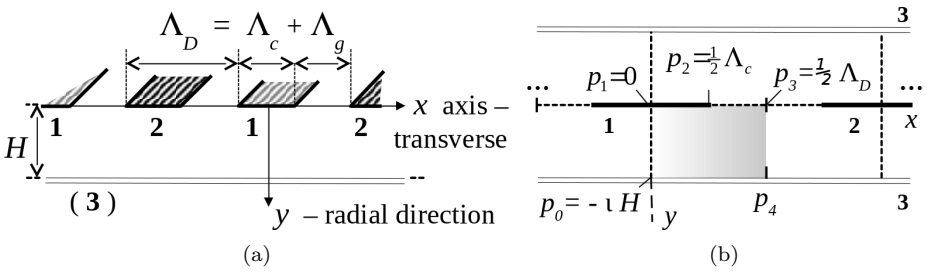

(a) (b)

Figure 2: Planar IDA fingers **1** and **2** on a strip with or without backside contact **3** (a), and shaded modeling quadrant or tile in physical $\boldsymbol{p}$-plane (b) with constant potential (—) or flux ($\cdots$) boundaries.

finally impedes treating interelectrodes coupling modes and layer-to-layer interfaces types differently – whereas they shall be distinguished. Strictly speaking, effective permittivities are global properties (one per crystallographic axis) issued from a unique or equivalent filling media. They should be deduced for a whole device from its end characteristics once computed [31]. By contrast, partial permittivities are solely P.C.-specific subsidiary notation and may then be dropped as such.

Running on from all of the above, our work derives a verified modeling straightforward framework with computability limits, which preserves as much as possible engineering insight while computing fast. Error levels are given and discussed but acceptability not much prescribed – for leaving users appreciate applicability with respect to their own constraints. Our multilayer composition is fundamentally though simply modified, using Kirchhoff laws of circuits theory rather than partial capacitances. It combines whole conductance values instead of separated permittivities and layers geometric ratios, and starts iterating from the outer-most layer instead of the inner-most. *Per-layer* effective permittivities are left aside, for not offering much benefit. Materials are considered isotropic and homogeneous, although effective-medium approximations may apply for main crystallographic axes aligned on the electrodes coordinates system [47, 55–57]. Eventually, our solution unravels through following milestones:

1. review poly-gap conformal mappings on monolayer;
2. reduce asymptotic formulas for thin and thick layer;
3. extract computational thickness thresholds;
4. express median-flux coordinates, said *isotropical*;
5. provide multilayer combination Kirchhoff algorithm;
6. report reliable finite-elements benchmarks;
7. demonstrate the approach on ISIT measurements.

2. Theory

Two coupled conductors on a plane surface define a coplanar device, called "strip" when a third contact is provided to the backside. Section 3.1 focuses

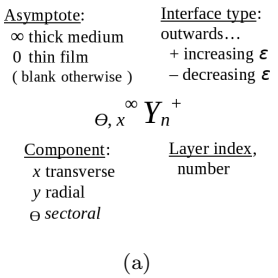

(a)

Single-gap poly-gap	Two-fingers pair; multiple-fingers IDA.
Transverse radial sectoral	Finger-to-finger; finger-to-backside; combinaison of both.
Iso- (-trop*ical*)	Mid-point between 2 regions of equal integrated flux.
Partial (capacitance)	Related to layers extension for stratified substrate decomposition.

(b)

Figure 3: Symbol used for main characteristics – here the admittance – with its 4-corners explanations (a), and elements of vocabulary (b).

on one interdigital gap of a fingers array (IDA) on a unique substrate layer as depicted by Figure 2. Presuming no potentials variation along the electrodes fingers (quasi-TEM, Transverse ElectroMagnetic approximation) allows accounting for the third geometrical dimension by an independent set of equations [58, 59] – which can reduce to a multiplicative factor. Putting aside finite-length array borders effects, the three-dimensional structure is then downgraded to an elementary cut from which the real device is simply considered extruded. Common symmetry heuristics separate upper and lower sides of the electrodes plan, such that a real device is usually modeled by assembling independently-solved half planes. Electrode thickness is also taken into account at early stage, either separately by means of simple parallel-plate formula [60], or merged with the upper side through more complex resolution [52, 56, 61], but most often tackled for being negligible through Wheeler's approximation [62].

In the perspective of Section 3.2 for multilayer substrate modeling, a back contact also stands for an interface to an attached material of higher admittance, including but not limited to perfect conductors, whereas a bare backside corresponds to an exposure to lower admittance such as an ideal insulator – with purely theoretical zero permittivity. For sharing same analytic transformations, coplanar and strip electrodes schemes will be considered through the same canvas, as well as mono- and multi-layer substrates.

A new notation proposal is thereby introduced as delineated in Figure 3, inspired by chemical elements representation, aggregating most of multilayer substrate electrodes modeling aspects. Left hand side super- and sub-scripts have been chosen to specify thickness-related asymptotic approximations and coupling component considered, respectively. Right hand superscript states boundary condition type as '+' for outward-increasing permittivity or back-contact presence, '−' otherwise. Lower-right corner holds layers numbering.

2.1. Lumped-elements formalism

As explained in Appendix A, electrodes voltages and currents are related through admittances proportionality factors – impedances inverses – noted ${}_yY$ for finger-to-backside radial coupling and ${}_xY$ for interdigital transverse component, illustrated in Figure 4. Combination of both has been called ${}_\theta Y$ *sectoral*

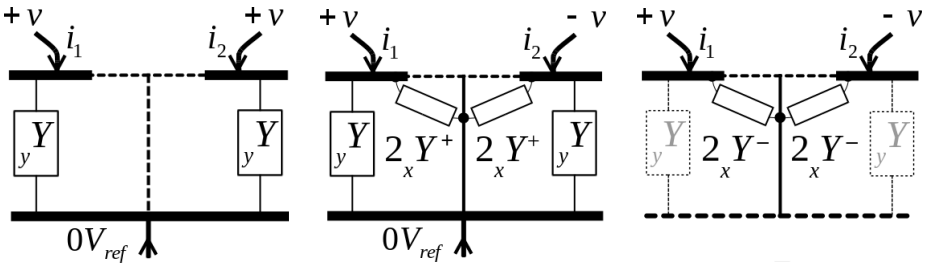

Figure 4: Lumped elements between electrodes (thick segments), constant potentials (—) and flux lines (⋯) according to mode.

coupling. By contrast with literature dedicated to radiofrequencies, *odd* and *even* symmetries or differential and common modes are preferably not named as such. This is because odd or differential mode evocation does not tell if a back-side contact is or not interacting with coplanar fingers (Fig. 4-b or -c), whereas distinguishing both cases is needed for multilayer combination. By consistency, even- or common-mode aren't promoted either. For naming electrodes polarization schemes and couplings principal orientations, qualifiers have been chosen as radial (even common-mode, Fig. 4-a), transverse (odd differential mode without back contact, -c) and *sectoral* then (odd differential mode with back contact, -b).

An admittance can be interpreted as issued from a complex capacitance C^* measured at frequency f: $Y = C^* \, \iota \, 2\pi f$, where ι is the imaginary unit. Capacitance is complex (star superscript) to include non-zero imaginary losses for dispersive or conductive compounds. Components are then expressed as products of filling material's ε^* complex permittivities and CSR cell shape ratios accounting for electrodes geometry and polarization schemes. Dropping C's star from now on, they will be written:

$$_{\theta,y}C \equiv \, _{\theta,y}\varepsilon^* \, _{\theta,y}CSR \quad \text{but} \quad 2 \, _xC \equiv \, _x\varepsilon^* \, _xCSR.$$

Last doubling factor has been put to profit from symmetry and spare divisions by 2, like in the following fundamental invariant – explained in Appendix (identity A.2):

$$_xCSR = \, _\theta CSR - \, _yCSR. \tag{1}$$

2.2. From boundaries to conformal mapping

Since capacitances evaluate as flux-over-field ratios, CSR are deduced from solving complex potentials around charges *loci* at substrate's boundaries – Laplace equation. Conformal transformations allow for such computation by mapping electrodes arrangements into a standard parallel-plates disposition, with analytical functions valid throughout the filling medium – assumed electrically uncharged.

Only one plane quadrant or tile is considered thanks to fingers assumed periodicity, after fixing likely symmetry clauses equally known as Dirichlet or Neumann conditions, equipotential or constant flux – hereafter called *isoflux* – boundaries, electric or magnetic walls, virtual close (short) or open. In particular, the hypothesis of fields symmetry about the electrodes plan presumes an isoflux on x-axis between fingers. Additionally, ${}_yC$ radial coupling comes with an isoflux on ordinates mid-axis, whereas ${}_\theta C$ and ${}_xC$ odd symmetry there virtually produces a grounded equipotential (*cf.* Figure 4).

Working out successive approximations and trigonometric developments leads to thin-film ${}^0CSR$ and infinite-medium ${}^\infty CSR$ asymptotes depending on ξ machine computation absolute tolerance, which is around 10^{-3}, 10^{-7} and 10^{-16} in half (16 bits), single (32) and double (64) precision, respectively. Although performances degradation is not expected from desktop computers, it is believed that low-precision computing could regain interest for innovative purposes like optimization or deep learning techniques [63, 64] helping more complex substrates classification for example [65, 66]. Also, if mental calculation could be seen as of half-precision, then the present approach would interest engineers looking for quickly estimating by hand some orders of magnitude.

3. Calculation

3.1. Monolayers analysis

Electrodes fingers gratings transformations in bidimensional cut start from an interdigital tile of the physical $\boldsymbol{p}$ plane as enlightened in Figure 2-b. Geometrical parameters Λ_c, Λ_g, Λ_D and H recall conductors width, interdigital gap, finger-to-finger periodicity and substrate height or thickness. Neglected borders effects due to finiteness of fingers number and length are discussed hereafter. Conformal mappings in forward sense – from $\boldsymbol{p}$ physical to $\boldsymbol{s}$ square-cells domains, and handier $\boldsymbol{p} \hookleftarrow \boldsymbol{s}$ backward equations sequence are detailed in Appendix B (Figure B.11 and Table B.1).

3.1.1. General case

Parallel-plates conformations resulting from Schwarz-Christoffel transformations permit self and mutual coupling ratios direct evaluation as:

$$
\begin{aligned}
{}_yCSR &= \frac{\mathrm{K}({}_yk)}{\mathrm{K}({}_yk')}\,, & {}_xCSR^- &= \mathrm{K}({}_xk)/\,\mathrm{K}({}_xk')\,,\\
{}_\theta CSR^+ &= \frac{\mathrm{K}({}_\theta k)}{\mathrm{K}({}_\theta k')}\,, & {}_xCSR^+ &= {}_\theta CSR^+ - {}_yCSR
\end{aligned}
$$

with

$$
\begin{gathered}
{}_\theta k = t_2\,,\quad {}_yk = {}_\theta k\,\kappa,\quad {}_xk = {}_\theta k\sqrt{\frac{1-\kappa^2}{1-{}_yk^2}}\\
\text{for}\quad t_2 = \mathrm{sn}\left[\tfrac{\pi\,\vartheta_3^2(q)}{2}\Lambda_c/\Lambda_D, \kappa\right] \text{ and } \kappa = \vartheta_2^2(q)\,/\vartheta_3^2(q)
\end{gathered}
\tag{2}
$$

where ${}_{...}k' = \sqrt{1-{}_{...}k^2}$ are complementary *moduli* in K( ) complete elliptic integrals of the first kind, $\vartheta()$ Jacobi *theta* functions of nome $q = e^{-\pi 2H/\Lambda_D}$, and sn() Jacobi's elliptic sine. Differential modes '+' superscript stands for strip conductor-backing explicitly, except for radial ratio ${}_yCSR$. The latter will indeed be used as it stands on any kind of interface for multilayer modeling (Section 3.2). Complementary identity ${}_\theta CSR^- = {}_xCSR^- + {}_yCSR$ (eq. 1) holds true for the same purpose.

Above equations correspond to those by Igreja & Dias [50, 67], with a further distinction of coupling components from Gevorgian [51]. See also Blume or Luther et al. [48, 68] for computing κ otherwise, and Supplementary Material for K-quotients approximations. All CSR expressed per interdigital gap should be multiplied by the actual IDA fingers length and number. Next, their asymptotes were derived from limit-case *moduli* expressions (Appendix B.1).

3.1.2. Thin film

As film thickness falls below about a few tenths of fingers periodicity, down to zero, nearly unitary ${}^0q$ in (2) yields infinite ${}^0\vartheta_2 \simeq {}^0\vartheta_3$ whose ratio ${}^0\kappa$, and subsequent ${}^0_{\theta,y}k$, saturate to unity (${}^0_xk$ to zero). Thin-film asymptotic ${}^0CSR$ have then been derived as:

$$\begin{aligned}
\forall \frac{H}{\Lambda_D} \leq \frac{-\pi}{2\ln(2\,\xi)}, & \\
{}^0_xCSR^- &\simeq \frac{\pi}{\ln\left(4\sqrt{2}\right) + \pi\frac{1}{2}\Lambda_g/H} \\
\text{or} \quad {}^0_xCSR^+ &\approx \frac{4}{\pi}\exp\left(-\pi\frac{\frac{1}{2}\Lambda_g}{H}\right), \\
{}^0_\theta CSR^+ &\simeq \frac{\ln(4)}{\pi} + \frac{\frac{1}{2}\Lambda_c}{H}\,; \\
\text{and} \quad {}^0_yCSR &= {}^0_\theta CSR^+ - {}^0_xCSR^+.
\end{aligned}$$

The threshold above corresponds to $H < \{25, 10 \text{ or } 5\}\%$ times Λ_D in half, single or double computing precision, respectively. Radial and sectoral ratios point to an equivalent width increased to about $\Lambda_c^e \cong \Lambda_c + 0.9H$ by fields residual fringing.

Blume et al. [48] further approximate ${}^0_xCSR^-$ linearly, without applicability criterion but with comparable performance (*cf.* Section 5.1.1). Vukadinovic et al. [31] ended-up on close ${}^0_xCSR^-$ based on parametric fit, for a single-gap device – parallel electrodes without IDA. Similar asymptotes may finally be derived from Transmission-Line expressions [69, 70], for thin multi-films in particular (*cf.* Section 5.1.2).

3.1.3. Thick medium

While approaching free-space limit, which means for $H > \{0.75, 2.2 \text{ or } 5.5\}\,\Lambda_D$ in half, simple or double precision, respectively

$$\forall \frac{H}{\Lambda_D} > -\frac{1}{2\pi}\ln(8\xi):$$

$$\overset{\infty}{_y}CSR \simeq \frac{\pi/2}{\pi H/\Lambda_D - \ln\left[\overset{\infty}{_{\theta,x}}k\right]}$$

$$\overset{\infty}{_\theta}CSR \cong \overset{\infty}{_x}CSR \approx \frac{\mathrm{K}\left[\overset{\infty}{_{\theta,x}}k\right]}{\mathrm{K}\left[\sqrt{1-\overset{\infty}{_{\theta,x}}k^2}\right]}$$

$$\text{where} \qquad \overset{\infty}{_{\theta,x}}k = \sin\left(\tfrac{1}{2}\pi\Lambda_c/\Lambda_D\right).$$

The sectoral component reduces to transverse-only well-known expression in infinite medium [46, 47, 67, 71], which cannot be further approximated. Back-side type doesn't much influence coupling fields anymore, such that no right superscript is indicated – it could as well be "+|−".

It is worth to recall that the radial asymptote assumes flux lines confinement between fingers – as presumed for interdigitated electrodes (Figure 2). While approaching array borders in real, finite devices, fields fringes would yet deploy laterally – the closer to border the wider. $\overset{\infty}{_y}CSR$ therefore looses acuteness as substrate thickness increases above a couple of times the entire array width $\{\Lambda_D$ times the number of gaps$\}$. One improvement would be to vary $\Lambda_c(x)$ and $\Lambda_D(x)$, as functions of the distance to array center, and then sum-up individually resolved gaps.

3.1.4. Isotropical coordinates

While odd-mode surface flux stands alone in infinite medium where no radial coupling exists, field fringes expansion towards the back contact inside moderately thick supports benefits to the radial component, such that transverse coupling ultimately fade out at thin film. Around an intermediate, particular case, radial and transverse equalizing fluxes significantly influence each-other. We describe as *isotropical* such thickness $_\theta H_\#$, as well as the *iso*-depth $\overset{\infty}{_{\theta,x}}H_\#$ equally separating near and far fields in infinite medium, defined as (*cf.* Supplementary Material):

$$_\theta H_\# = 0.56\Lambda_D\sqrt{\frac{\Lambda_g}{\Lambda_D}} \quad \text{and} \quad \overset{\infty}{_{\theta,x}}H_\# = 0.40\Lambda_D\sqrt{\frac{\Lambda_g}{\Lambda_D}}.$$

Both references come in complement to thin-film and thick-support limits as noteworthy cases studies. They correspond in particular to transverse coupling highest relative sensitivity with regards to first-layer thickness relative variation [1]. Similarly, we evaluated the *iso*-width corresponding to the edge portion of an electrode finger that concentrates half of its total flux (near field), as:

$$\overset{\infty}{_{\theta,x}}\Lambda_{c\#} \approx \tfrac{1}{2}\Lambda_c - 0.42\Lambda_D\left[\sin\left(\frac{\pi}{2}\frac{\Lambda_c}{\Lambda_D}\right) - \tfrac{1}{4}\sin\left(\pi\frac{\Lambda_c}{\Lambda_D}\right)\right].$$

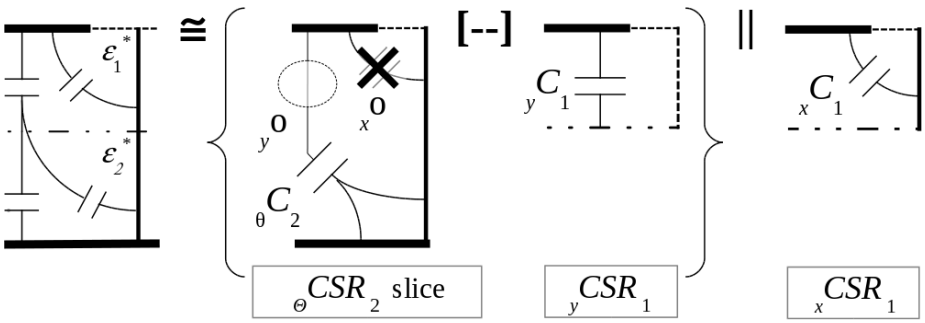

Figure 5: Developped "Partial-Capacitances" generalization illustrated for a bilayer with back contact in sectoral mode [1]. Symbols || and [- -] identify parallel and series association, respectively.

Practical significance of these coordinates are enlightened in Section 5.1.1 and Appendix B.2.

3.1.5. Finite arrays and single-gaps

Presented equations apply to infinite arrays, neglecting borders. For a pattern of N_g gaps, along x transverse direction, authors combine single- and poly-gap equations at each border in supplement to remaining $(N_g - 2)$ poly-gaps [Igr11, Bao19]. This was implemented by Pampin as well [1], which further details single-gap asymptotes, computability thresholds and *isotropical* coordinates. Such distinction may be needed for few gaps but not much above half a dozen, where including borders in main pattern commits less than ten percent error at worst (4 % average). In z direction now – at finger's end – Beilenhoff *et al.* [59, 72] propose a simple approximation. Provided same gap at the extremity as along one finger, extrusion length l_{fing} is grown with $(\Lambda_c + 2\Lambda_g)/4$, keeping 2D-cut ratios unchanged.

3.2. Multilayer combination

Stratified substrate calculations can be tackled by "partial-capacitances" (P.C.) techniques [31, 49], derived from the method of images [73] (schematic diagram in Supplementary Material). In short, Laplace equation is resolved inside each interior stratum as if it had been extended to reach the coplanar electrodes surface, thus decomposing the problem into monolayer cases – numbered $n \in [1..N_s]$ for N_s layers. Excessive parts introduced by layer extensions are withdrawn, and individually solved components re-wrapped together according to inter-layers boundary conditions: parallel combinations for outwards-decreasing permittivities (PPC), series for increasing (SPC). In n^{st} layer of thickness T_n, evaluations of C_n assume an homogeneous filling material, continuous from coplanar patterns to n^{th} interface, at cumulative distance $H_n = \sum_1^n T_n$.

Stretched parts contributions are usually withdrawn via so-called "effective" or *partial* permittivities prescaling as detailed in Appendix C: inwards sub-

tracting $\varepsilon_{(n-1)..1}$ in monotonic PPC or their inverse in SPC [49, 50, 53, 56]. Both make physically sense for two-contacts canonical schemes (Appendix Figure C.13) and will serve as starting base for our generalized algorithm. At this point however, PPC is not meant to deal with a backside contact, nor SPC with lower internal permittivities. Blume et al. [48] include CSR_n factors in partial permittivities calculation to circumvent such limitations. But this doesn't take exterior interfaces flux fully into account, since iteration is done on adjacent layers in an improper direction – from coplanar pattern to the outside. This doesn't either separate transverse (finger-to-finger) and radial (finger-to-backside) coupling components as needed to characterize a device with back contact. Neither PPC nor SPC alone applies to coplanar-strips in sectoral mode for example, which combine transverse and radial couplings. The electromagnetic flux therein swings between one or the other preferential direction depending on substrate thickness and inter-digital gap width (see Appendix Figure B.12). Partial images and alternative ("projected stripe" [51]) are further discussed in Supplementary Material.

In our work, whole ($\varepsilon_n\, CSR_{n-1}$) extruded parts are explicitly subtracted or "de-serialized" from C_n components. This is equivalent to partial permittivities for trivial stacks but allows treating transverse, radial and sectoral couplings differently for relatively thin layers (*e.g. isotropical*) forming non-monotonic stacks of permittivities. In such case indeed, multiple outward interfaces can influence internal fields balancing. From a transmission line point-of-view now, stacked layers form series-mounted quadripoles [74, 75]. Depicted as a ladder shape, transverse couplings would form rungs between radial jambs. Following Kirchhoff laws, substrate can then be rolled up in sequence from its outermost side to the coplanar electrodes surface, incrementing the outer stack equivalent load at each step by inner coupling components. Figure 5 illustrates the process for a bilayer coplanar-strip: ${}_{\theta}C_{n+1}$ wraps in series with radial ${}_{y}C_n$ and parallel with transverse ${}_{x}C_n$, but only after eliminating image-related ${}_{x,y}\mathrm{o}$ extended parts. The algorithm may be implemented according to quadripoles chaining theory, in short building each layer's transmittance 2x2 matrix and performing their product. A more explicit iterative loop is given here, using ${}_{\theta,y,x}\mathrm{A}$ temporary variables to store intermediate admittances values. Starting inwards from the outside medium or back-contact terminal, initiating ${}_{\theta,y}\mathrm{A}_{N_s} = {}_{\theta,y}C_{N_s}$, our general algorithm can be written:

for $n = (N_s - 1)$ *down-to* 1,
do

$$
\begin{aligned}
{}_{y}\mathrm{o} &= \varepsilon^{*}_{n+1}\ {}_{y}CSR_n \\
{}_{y}\mathrm{A}_n &\leftarrow \left[\frac{1}{{}_{y}\mathrm{A}_{n+1}} - \frac{1}{{}_{y}\mathrm{o}} + \frac{1}{{}_{y}C_n}\right]^{-1}
\end{aligned}
$$

$$
\begin{array}{l}
|\varepsilon_n^*| < |\varepsilon_{n+1}^*| : \\
\qquad \left|
\begin{array}{l}
\quad {}_x\mathrm{o} = \varepsilon_{n+1}^* \; {}_xCSR_n^+ \\
{}_\theta\mathrm{A}_n \leftarrow \left[\dfrac{1}{{}_\theta\mathrm{A}_{n+1} - {}_x\mathrm{o}} - \dfrac{1}{{}_y\mathrm{o}} + \dfrac{1}{{}_yC_n} \right]^{-1} \\
\qquad\quad + 2\,{}_xC_n^+ \\
{}_x\mathrm{A}_n \leftarrow {}_\theta\mathrm{A}_n - {}_y\mathrm{A}_n
\end{array}
\right. \\
|\varepsilon_n^*| > |\varepsilon_{n+1}^*| : \\
\qquad \left|
\begin{array}{l}
\quad {}_x\mathrm{o} = \varepsilon_{n+1}^* \; {}_xCSR_n^- \\
{}_x\mathrm{A}_n \leftarrow {}_x\mathrm{A}_{n+1} - {}_x\mathrm{o} + 2\,{}_xC_n^- \\
{}_\theta\mathrm{A}_n \leftarrow {}_x\mathrm{A}_n + {}_y\mathrm{A}_n
\end{array}
\right.
\end{array}
$$

done

$$
\textit{return} \quad {}_{\theta,y}C_{(0)} \leftarrow {}_{\theta,y}\mathrm{A}_1,\ {}_xC_{(0)} \leftarrow \tfrac{1}{2}{}_x\mathrm{A}_1,\ \varepsilon_{\mathrm{eff}} = \frac{{}_\theta C_{(0)}}{{}_\theta CSR_n}.
$$

Resulting $C_{(0)}$ components are the 2D admittances per gap and fingers length unit. Effective permittivity $\varepsilon_{\mathrm{eff}}$ is given for the whole device – neglecting borders peculiarities. Implementation-wise, corrected terms involving $\{{}_y\mathrm{o}\ ;\ {}_yC_n\}$ and $\{{}_x\mathrm{o}\ ;\ {}_xC_n\}$ could employ partial permittivities using the ${}_{y,x}C_n$ developed in Appendix C, for ${}_y\mathrm{A}_n$ and ${}_\theta\mathrm{A}_n$ in particular. Identity (1) can be recognized in $\{{}_x\mathrm{A}_n\}^+$ and $\{{}_\theta\mathrm{A}_n\}^-$ as an invariant, always maintained.

The most obvious difference with other P.C. approaches is the differentiated treatment applied to transverse and sectoral components depending on interface type, allowing to mix parallel and series combinations for non-monotonic profiles. Reverse iteration keeps accounting for distant interfaces currents and subsequent voltage drops, across layers, from the outside to the coplanar surface and up to the device cut global parameters.

4. Materials and methods

4.1. Numerical benchmarks

The analytical model has been programmed and tested under MATLAB® and Scilab. For intensive verifications on perfect reference structures while addressing computational inaccuracies, multiply checked simulations by finite-elements (F.E.) were first preferred to scarce discretionary measurements. About two thousand numerical runs were processed in that regard by means of scripting. Professional semiconductor-oriented software (Synopsys® Sentaurus™ suite) was used for its broad tuning capabilities of mesh parameters, materials properties and perfect-conductor or ideal-insulator boundaries. Substrate materials are considered pure dielectrics with permittivities given relatively to empty-space reference $\varepsilon_0 = 8.9\,10^{-12}$ F/m.

A rectangular 2D cut is simulated ('SDE' drawing tool), laterally delimited at fingers' centers and containing an even number of them. With one pair typically, as in Figure 4, the whole domain spans Λ_D in width and H total

height – possibly including strata for multilayers. The outside is not meshed, and Neumann boundary condition applies to all four borders (except at fingers and back-contact elements – Dirichlet there). Such an ideal isolation is not physically realistic, for thin layers more notably, but permits to verify model theory at the layer scale – including limit cases – before passing to multilayer combinations. Different mesh refinement regions are setup ('Sentaurus' Delaunay axis-aligned generator): one over each layer, under each electrode finger, and for the interdigital gap. As detailed in Supplementary Material, refinement targets are specified as fractions of widths, thickness(es) and *isotropical* landmarks. Refinements needs for minimizing F.E. errors were assessed by preliminary trials. Several dozens up to a hundred thousand vertices were required for taking worst-cases errors down to a few percents, in transverse more particularly – through the interdigital gap. This mostly depends on Λ_g/Λ_D: about 40 k vertices are necessary under the 0.5 ratio, but above two times more in $0.8 \ldots 0.85$. To get the admittance matrix ('sdevice' tool), mixed-mode 'ACCoupled' plugin was used with Poisson and electrons continuity equations at 1 kHz, the two latter being though not critical for insulators simulation. Solver was left as default (Supernodal direct linear engine, using Block decomposition) but its precision extended to 256 bits. Capacitances were extracted by post-processing ('Inspect').

In terms of tests coverage and plots resolution, Λ_g/Λ_D values have been taken as 7 samples along a linear scale from 0.02 to 0.98. Swept thicknesses have been sampled as 14 log-scaled values in ranges that are specified for each test case in Section 5.1.

4.2. Sensors on silicon

Design and fabrication of the ISIT introduced in Figure 1 were detailed by Pampin et al. [1, 28]. Shortly, 300 nm-thick aluminum interdigitated electrodes were patterned as $\Lambda_D = 4$ µm, $\Lambda_g/\Lambda_D = 0.5$, 84-gaps square arrays on a substrate and covered by 70 nm alumina (Al_2O_3). Thin 31 nm silicon dioxide (SiO_2) insulates the IDA from 100 nm silicon film (Si), N-type doped at $2 \cdot 10^{16}$ phosphorous atoms/cm^3 and floating on 300 nm-thick depleted Si, over 650 µm P^--type Si, lightly doped at 10^{15} boron/cm^3 and equipped with backside ohmic contact. Electrodes access lines and contact pads round the IDA are furthermore insulated from substrate by 300 nm SiO_2 to lower peripheral couplings and parasitics. Pads are on top protected against Al_2O_3 passivation to allow probing.

Silver balls (Ag diameter ø 0.7 µm) were crystallized on the Al_2O_3 surface by liquid-phase processing of bare dies holding ISITs, for specifically revealing Deoxyribo-Nucleic Acids (DNA) hybridization as detailed by Moreno et al. [30, 76]. After functionalization with 7-octenyltrichlorosilane, 30 fmol of 120-mer DNA single strands were spotted on the IDA with a grounded metallic tip on micromanipulator under optical microscope. Hybridization at trappers' end with complementary targets inside multibiotinylated 534-mer strands then collects gold 20 nm particles coupled to antibiotin antibodies. Finally, Ag-enhancement follows silver nitrate catalyzed reduction on gold [77]. Biochemical residues of

silanes layers, DNA and biotin markers were not considered leaving more than a few nanometer dried layers, finally neglected.

Once dried, devices were measured by an LCR meter (Agilent 4284-A) setup at 0.1 V signal amplitude, long integration time and 8× averaging. As visible in Figure 8-a, Section 5.2, IDA pads were doubled to reinforce repeatability; unused lateral planes were left floating after checking they had no influence – thanks to thicker insulation. For open-calibration, probe pads and access tracks without central IDA were used on each die and spotted as well. No significant influence of the biochemistry was measured there, as the Ag layer is not dense enough to reach percolation and short-circuit the accesses.

5. Results and Discussion

5.1. Benchmark simulations

5.1.1. Monolayers

Conformal model's errors with regards to F.E. are shown in Figure 6 for a single layer with perfectly conducting or insulating backside, respectively – the latter said "without back contact". Support thickness ranges from 1/10 to 20 times the fingers periodicity, to challenge our model up to the 64 bits computing limits. In nominal area where no asymptote is used, radial and transverse errors fall below 5 %. Isotropical thicknesses turn out to well indicate computing difficulties toward the low-thickness regimes. Below 20 % still, worst discrepancies are observed on insulated backside for the narrowest gaps, where thin film approximation fails (Fig. 6-c).

Errors originate in our asymptote – not in F.E. benches – as tested by emulating machine half precision $\xi = 10^{-3}$ in our model, which led to the same error at same corner (Fig. 6-c′). By moving thin and thick layer thresholds closer to each-other, this test meanwhile suggests that asymptotes-only models may be used for $10\,\% \leq \Lambda_g/\Lambda_D \leq 90\,\%$, in applications tolerant to 3 dB errors typically, sparing elliptic integrals computation [78].

Prior art by Blume et al. [48] was evaluated for comparison, featuring a simpler transformations sequence. Its merits under open backside are similar to ours (Figures in Supplementary Material) except at the thin-film and narrow-gap corner, where our approximation has three times less error. However, the case with back contact could not be assessed positively. This is likely due to the change in structure connectivity used to emulate functional modes. Discarding or not the back contact alters the admittance matrix and compromises coupling components extraction. Moreover, transverse evaluation there was improperly taken from the open backside, and radial coupling was not given. Other prior-art recursive images [54] were also considered, although they are not meant to deal with ideally-insulated monolayers as done here. Heavier computations are needed to cover all cases, especially radial coupling in thick layer, as well as mesh optimization. An open monolayer has yet been emulated (Figure in Supplementary Material), showing additional difficulties at thin films and wide gap – maybe due to the mesh. Because such numerical method differs from our

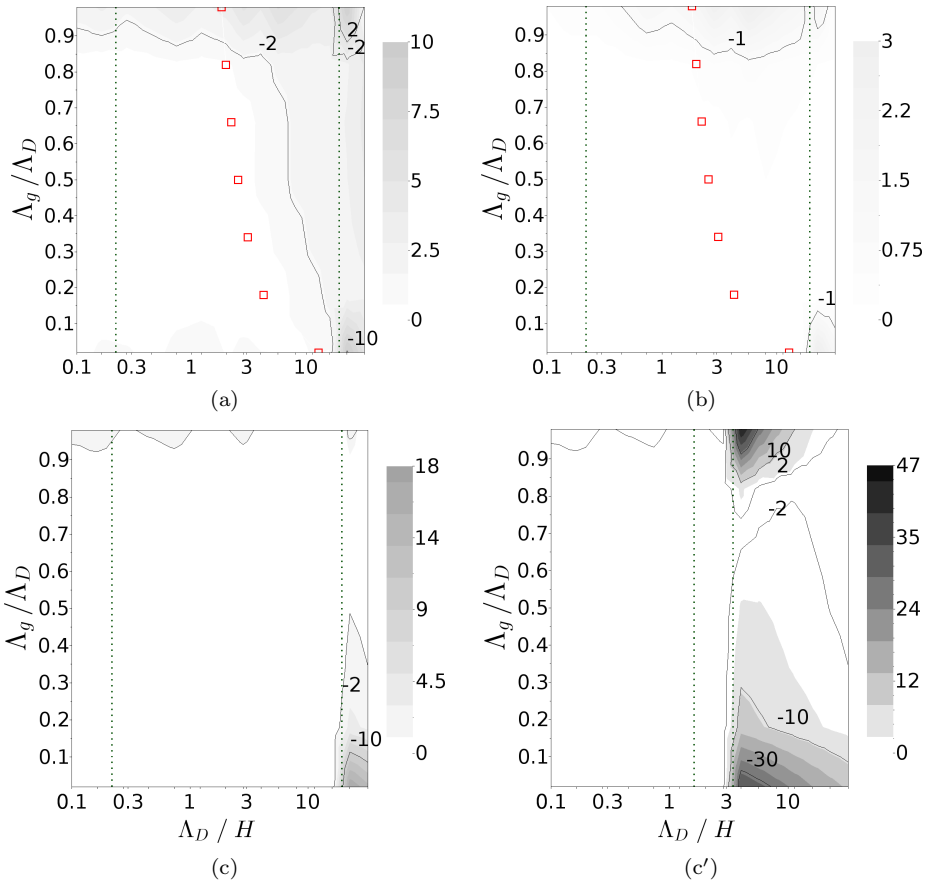

Figure 6: Monolayer analytical model errors relative to F.E. verification benches. With a back contact (a–b) : transverse (a) or radial (b) errors. Without back contact (c–c′): transverse-only errors under double (c) or half (c′) computation precision. Shades of gray and isocontours both indicate error values [%]. Dotted lines delimit thick or thin layer regimes; squares locate *iso*-thicknesses. Figures made of 14 × 7 tests (abscissa × ordinates); $\Lambda_D = 1$ µm, $\varepsilon = 1$.

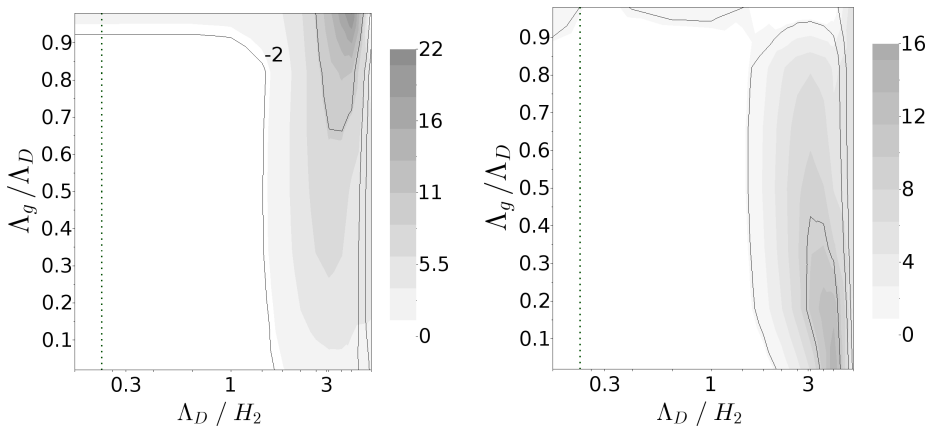

Figure 7: Three-layers transverse-only errors *vs.* F.E. ($\Lambda_D = 1$ µm). Radial errors not shown for being below 1 % everywhere. Dielectric stacks are (a) $\varepsilon = \{3\ 1\ 3\}$ on open backside, or (b) $\varepsilon = \{1\ 3\ 1\}$ closed on a back contact. Dotted lines delimit thick layer regimes.

close-form approach, investigation were not pursued at that point. A bilayer is still discussed at the end of Section 5.1.2.

5.1.2. Multilayers

Three-interfaces substrates with alternating permittivities have then been evaluated. Specific dielectric vectors are detailed under the figures discussed below, and a drawing provided in Supplementary Material. Second layer of constant thickness $T_2 = 0.2\,\Lambda_D$ is slided at variable depth in a stack of total height $H = 6\,\Lambda_D$, also constant. Layers 1 and 3 filled with a common medium have thicknesses varying between 0 and $(H - T_2)$. At these bounds, $T_1 = 0$ or $T_3 = 0$, two kinds of bilayer stacks are then also tested occasionally. Contrarily to other works (*e.g.* [31]), permittivities ratios between layer 2 and its surrounding were chosen moderate rather than high, for providing worse-cases errors (not shown 1:10 ratios were also evaluated). Inter-layer boundary conditions are less tightly verified and thereby more challenging for the cases shown here.

Precision is achieved even at thin first film and narrow fingers width or gap (Figure 7): above 75 % on open backside (-a) and 80 % with back contact (-b). As limitation, having more than one thin layer just under the electrodes has been experienced to bring transverse error close to 100 %, particularly with a back contact. Since this happens by forcing $\xi = 10^{-3}$ half-precision in our model, root cause most likely resides in ${}^{0}_{x}CSR^{+}$ approximation and not in the multilayer combination. A candidate improvement could call for combining thin-film asymptotes with Transmission-Line Models, in function of thickness regimes and interfaces quality, addressing fluxes crowding along vertical or horizontal axes [69, 79, 80]. By comparison, Blume's partial permittivities [48] were also evaluated (Figures in Supplementary Material). Without backside

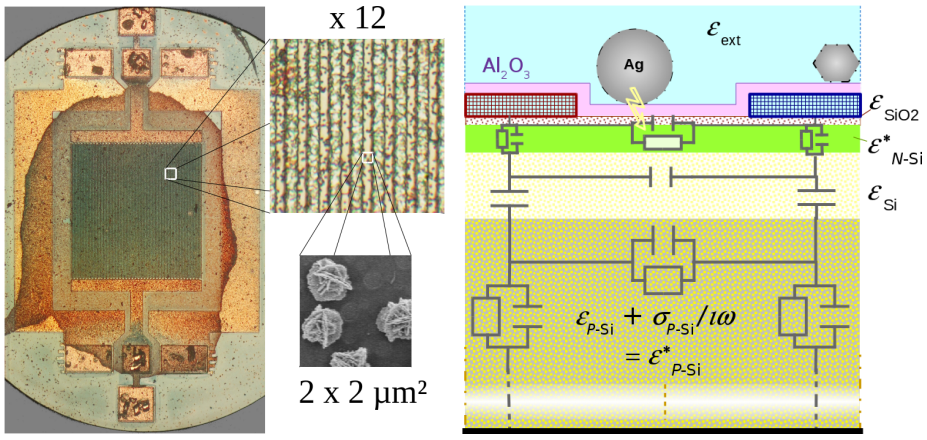

(a) (b)

Figure 8: ISIT-bulk for Ag labels detection. (a) probe pads layout and IDA covered by Ag spot; (b) fingers pair and gap cross-section in Ag grain detection by field effect on insulated semiconductor – 30 nm SiO_2, 100 nm N-type Si, 300 nm depleted Si, and 600 µm P^--Si.

contact, they commit about 20 % error on regular cases while not managing thin films correctly; with a back contact, they well manage thick layers only. As earlier stated, their limitations mainly originates from wrong layers iteration and no individuation of couplings. Recursive images [54] were finally tried out, which resolve complex potentials for both sides of the IDA surface. They rely on meshing – at implementation overheads – and *ad-hoc* numerical integration for the capacitance. Results otherwise equal to ours are further discussed in Supplementary Material, but no evaluation for more than one interface could be reproduced as the algorithm implemented did not converge.

5.2. ISIT measurements

For final utility demonstration, analytical modeling has been confronted to early measurements of Insulated Semiconductor Impedance Transducers sensing metallic sub-micro-particles in dry air (*cf.* Section 4.2). The ISIT has been depicted in Figure 8 with lumped-elements superimposed for functional understanding (-b). Grafted conductive particles on the transducer modulate its N-Si channel resistance below the SiO_2 oxide, the highest the coverage the greatest the modulation [28]. Depleted Si – low conductivity – region further insulates the channel from P^--Si bulk and back contact. Surface electrodes sense the external medium on one hand, the variable-resistance channel through the oxide on the other. Two sets of equations are therefore solved for external-medium and substrate half planes, and both solutions finally summed. Channel and bulk have complex permittivities $\varepsilon^*(\omega) = \varepsilon - \iota\,\sigma/\omega$, where ι is imaginary unit and $\omega = 2\pi\,f$ pulsation at test signal frequency f.

Real permittivities ε and conductivities σ for SiO_2 oxide, depleted-Si region,

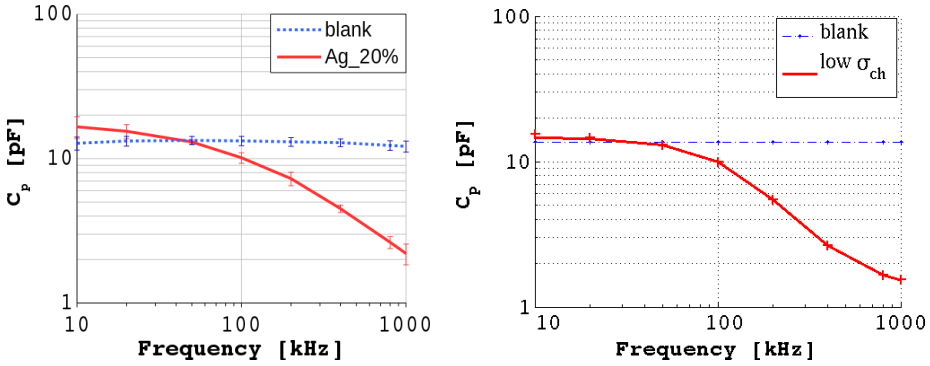

Figure 9: ISIT-bulk capacitance C_p – admittance imaginary part divided by pulsation – as measured (a) and computed by our model (b). Vertical bars in (a) indicate ± 1 standard deviations around 3-devices averages. Silver coverage is given in percentage of transducer's area. (b) Related channel's $\sigma_{\text{ch}} \equiv \sigma_{N\text{-Si}}$ influence.

P^--Si bulk and N-Si channel are:

$$\varepsilon_{\text{SiO}_2} = 3.9 \;\; [\,\varepsilon_0\,] \qquad \sigma_{P^-\text{Si}} = 3 \;[\text{S/m}]$$
$$\varepsilon_{\text{Si}} = 11.9 \;[\,\varepsilon_0\,] \qquad \sigma_{N\,\text{Si}} = \{10^2 \;;\; 0.01\}\;[\text{S/m}]$$

External ε_{ext} also increases with Ag coverage [30], from 1 (air) to 10. Given for zero and 20 %-Ag coverage, channel's $\sigma_{N\text{-Si}}$ were first estimated through auxiliary F.E. simulations and other mathematical physics [1], then ultimately fine-tuned to measurements. Multilayer interfaces types are evaluated at each frequency according to the $|\varepsilon_n^*(\omega)|$ modules (see Section 3.2 algorithm).

Figures 9 and 10 show a good agreement between model and measurements, in terms of variation range and capacitance cut-off frequency. Note that G_p conductance is taken in absolute value (Fig. 10), since it can seem negative in our model as in measurements [81], due here to the 3-terminals multilayer structure. Successive triangle-star transformations can indeed show that real-positive lumped elements lead to negative characteristics under certain conditions – out of scope here. Standard deviations were finally replaced by half the difference of third and first quartiles, a statistical measure of median spread less sensitive to extremes, to prevent negative values in dispersion bars as well. Low-frequency capacitance is dominated by the thin SiO_2 but also changes according to the external medium (Fig. 9). In presence of Ag grains, the latter becomes the main contributor at higher frequency due to substrate cut-off. Ag field effect indeed depletes the N-Si film from its free electrons, openning the initially conductive semiconductor channel. The same interpretation arises from G_p characteristic but requires another identification scheme – in series – going beyond present demonstration. Measurements variability there (Fig. 10-a) is associated with noise, usually higher in ohmic losses than in capacitance – averaging by nature. At low frequency, $||G_p||$ is however much higher than expected theoretically (Fig. 10-b). This likely originates in IDA passivation degradation, which could

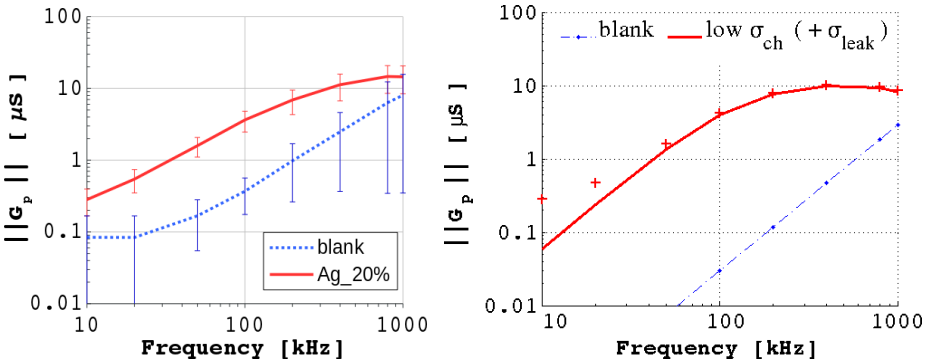

(a) (b)

Figure 10: ISIT-bulk apparent conductance G_p – admittance real part – in absolute value; (a) measured and (b) modeled. (a) Vertical bars report spreads around 3-devices means; Ag coverage is relative to transducer's area. (b) Influence of channel's $\sigma_{\text{ch}} = \sigma_{N\text{-Si}}$, with σ_{leak} leakage contribution ('+' markers) or without (plain line).

be modeled as an additional leakage in the external medium. Such artifact is hazardous, but a conductance σ_{leak} up to 40 µS/m distributed in about half a micron – Ag thickness taken as reference for convenience – already provides a fitting offset (Fig. 10-b cross marks).

Putting this work back into perspectives would finally call for a few more remarks. First, modeling has been focused on the characteristics of substrates in 2D (xy) cut. It voluntarily keeps aside ISIT particles statistics and field-effect magnification that explain full channel cut-off in 3$^{\text{rd}}$ dimension [1]. Second, simulated devices are perfect stacks of relatively simple materials without trapped charges, moisture sensitivity and other contingencies encountered in practice. Third, depleted Si layer's shape, thickness and depth are also slightly modified by surface particles field effect while considered constant in our model. Those close the loop for supporting and justifying present publication, that is: providing reliable formula and efficient algorithm for multilayer analysis in order to let physicists pursuing further modeling efforts, at other scales.

6. Conclusion

Wide-range analyses of planar interdigitated electrodes on multilayer substrates have been exposed, for poly-gap fingers arrays more particularly. Focus has been put on computability related to support thickness and on numerical verification, for bidimensional cuts reliable modeling. Beyond revisiting some known equations, our monolayer section provides thin-film and thick-medium asymptotic formula with their computation thresholds. Newly introduced *isotropical* coordinates further allow highest-field regions straightforward identification for sensors design. Our multilayers approach then generalizes "partial-components" techniques while being thoroughly verified for complex permittivites of increasing, decreasing or intermixed modules up to 4 distinct

layers. The proposed method reaches an improved compromise between algorithmic complexity and physical rightfulness. Experimental validation has on top been illustrated with measurements of ISIT, advanced semiconductor-based transducer. Sub-microparticles detection there produces more than one order of magnitude impedance changes, which can further be studied with confidence on the base of our robust model.

7. Acknowledgments

Authors are grateful to the *Région Wallonne* and FRS-FNRS, Belgium, for related fundings. The first author thanks all his relatives for support. *Libre* software were used in this work such as GNU/Linux and Scilab; model scripts have been made public as well [1] (for Matlab®).

Appendix A. Admittance matrix formalism

On a passive support, 3-ports passive devices global admittance can be described in terms of a symmetric matrix relating contacts v voltages and i incident currents following Ohm's law:

$$\begin{bmatrix} i_1 \\ i_2 \\ i_3 \end{bmatrix} = \begin{bmatrix} Y_{11} & Y_{12} & -\frac{1}{2}Y_{33} \\ Y_{12} & Y_{11} & -\frac{1}{2}Y_{33} \\ -\frac{1}{2}Y_{33} & -\frac{1}{2}Y_{33} & Y_{33} \end{bmatrix} \begin{bmatrix} v_1 \\ v_2 \\ v_3 \end{bmatrix}, Y_{ij} \equiv \left.\frac{i_i}{v_j}\right|_{v_{k\neq j}=0}$$

where subscripts $\{1, 2\}$ and $\{3\}$ refer here to coplanar electrodes and to backside – third column and row are null if back contact is absent. Single-node Y_{11} or Y_{33} respectively stands for finger or back-contact self-coupling factor, with others grounded, whereas Y_{12} characterizes finger-to-finger mutual component. When $v_1 = v_2 = v_3$, currents conservation law requires:

$$Y_{11} + Y_{12} - \frac{1}{2}Y_{33} = 0. \tag{A.1}$$

Above relations hold true for any structure enclosing no inner charge – *i.e.* satisfying Laplace equation – regardless of characterization practices. Theoretical modeling benefits from symmetry by noting, for driven $v_3 = 0$ and v_2 proportionnal to v_1:

$\left.\frac{i_1}{v_1}\right|_{\substack{v_2=v_1 \\ i_2=i_1}} = Y_{11} + Y_{12} = {}_yY$ common-mode finger coupling with backside;

$\left.\frac{i_1}{v_1}\right|_{\substack{v_2=-v_1 \\ i_2=-i_1}} = Y_{11} - Y_{12} = {}_\theta Y$ finger to grounded tile *sectoral* parameter (Figure 4).

In matrix terms, ${}_yY$ and ${}_\theta Y$ eigenvalues correspond to $[v; v; 0]^{\mathrm{T}}$ (double) and $[+v; -v; 0]^{\mathrm{T}}$ eigenvectors in even and odd parity, respectively. In former case, ${}_yY = \frac{1}{2}Y_{33}$ identity follows from equation (A.1) and transverse finger-to-finger component along x direction returns as following difference:

$${}_xY = -Y_{12} = \frac{1}{2}\left({}_\theta Y - {}_yY\right), \tag{A.2}$$

which expresses flux conservation between contacts.

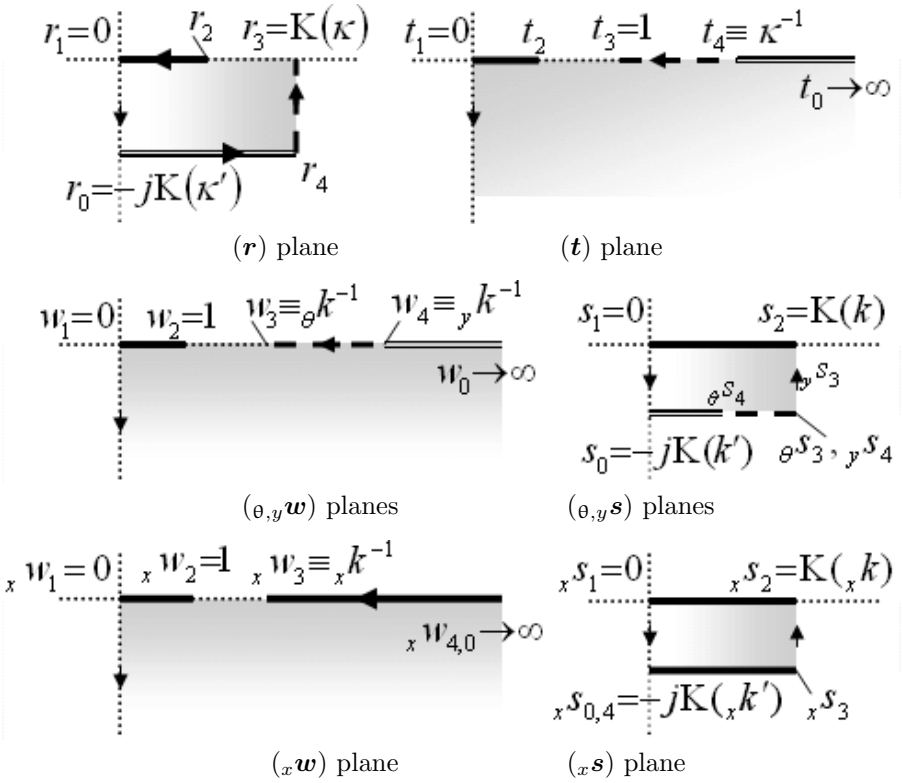

Figure B.11: Interdigital cut conformal maps: the physical $\boldsymbol{p}$ tile, prescaled into $\boldsymbol{r}$, is unfolded to $\boldsymbol{t}$ then rescaled as $\boldsymbol{w}$ and folded back into $\boldsymbol{s}$ ideal parallel plates. Finger-to-backside coupling is treated in radial ${}_y\boldsymbol{s}$, finger-to-mid-axis in transverse ${}_x\boldsymbol{s}$, and both in sectoral ${}_\theta\boldsymbol{s}$. Dashes depict a virtual ground for ${}_\theta\boldsymbol{w}$, but an isoflux axis for ${}_y\boldsymbol{w}$. Plain arrows describe an arbitrary walk for reference.

Appendix B. Schwarz-Christoffel mappings (SCM)

Following Igreja & Dias [50, 67], conformal transformation from the electrodes fingers pair $\boldsymbol{p}$ domain to a parallel-plates $\boldsymbol{s}$ slab calls for $\boldsymbol{r}$ prescaling followed by $\boldsymbol{t}$ and $\boldsymbol{w}$ intermediate flattening. Identifying $\boldsymbol{p}$ vertices with SCM integrand poles in $\boldsymbol{r}$ allows one tile forward unfolding to $\boldsymbol{t}$-plane lower half (Appendix Equations B.1-B.2). Normalizing by finger's edge t_2 abscissa to form $\boldsymbol{w}$ plane finally precedes another SCM folding back to $\boldsymbol{s}$ (eq. B.3-B.4). Incomplete elliptic integrals of the first kind there involve *moduli* (Equation 2):

$$ {}_\theta k = t_2\,, \quad {}_y k = \frac{t_2}{t_4} = {}_\theta k\,\kappa, \quad {}_x k = t_2\sqrt{\frac{t_4^2-1}{t_4^2-t_2^2}} $$

$$ \text{for } t_2 = \mathrm{sn}\left[\tfrac{\pi\,\vartheta_3^2(q)}{2}\Lambda_c/\Lambda_D, \kappa\right] \text{ and } t_4 = \frac{1}{\kappa} = \frac{\vartheta_3^2(q)}{\vartheta_2^2(q)}. $$

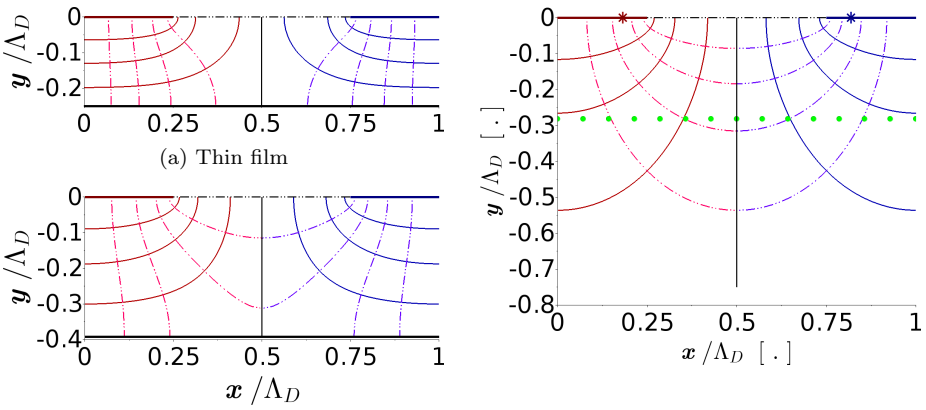

(a) Thin film

(b) *Isotropical* layer

(c) Thick medium

Figure B.12: Complex potentials stepped by 1/4 and 1/5 of electrode's v voltage and i current, respectively. (c) Dots highlight *iso*-depth ${}^{\infty}_{\theta,x}H_{\#}$ and fingers edge *iso*-width ${}^{\infty}_{\theta,x}\Lambda_{c\#}$.

Appendix B.1. Moduli computability conditions

Asymptotic developments constitute the most laborious but essential process that provides thickness limits around which close-form approximations become necessary, considering elliptic integrals computability issues at nearly null or unitary *moduli*. Computability thresholds evaluation starts from either k or k' complement, a non-unity criterion on k' being safer for ensuring k non-nullity as well, that is: $(k' \leq 1-\xi) \Leftrightarrow \left(k \geq \sqrt{2\xi}\right) \Rightarrow (k > \xi)$.

Consult Supplementary Material for calculation details.

Appendix B.2. Plots

Figure B.12 fringing fields plots demonstrate general backward equations (B.4) to (B.1) on a layer of *isotropical* thickness, after $\mathrm{F}(\varphi, k)$ arithmetic-geometric mean computation [44], as well as thin-film and thick-support asymptotic cases. Variable ${}_{\theta}s$ is swept in the complex plane comprised between 0 and $\mathrm{K}({}_{\theta}k) - \iota\,\mathrm{K}({}_{\theta}k')$, then mapped to p domain. When restrained to x–y principal axes, Table B.1 close-forms also ease localization of relevant coordinates beyond which radial or transverse coupling falls down to a little portion of the whole, useful for device design and meshing refinements specification [1].

Appendix C. Bilayer canonical partial capacitances

Strictly coplanar fingers – with no backside contact – show transverse-only differential fluxes considered parallel, which justifies admittances addition in PPC [17, 46, 48, 53, 67, 82]: ${}_{x}C = {}_{x}C_2^{-} + {}_{x}\Delta_1^{-}$ (Fig. C.13-a). On a back-contacted strip, the radial flux reaching distant layers doesn't flow along their

Case – General	Thin	Thick	
$\boldsymbol{p} = \Lambda_D \dfrac{\boldsymbol{r}}{\pi\, \vartheta_3^2(q)}$	$H \dfrac{{}^{0}\boldsymbol{r}}{\pi/2}$	$\Lambda_D \dfrac{{}^{\infty}\boldsymbol{r}}{\pi}$	$(B.1)$
$\boldsymbol{r} = \mathrm{F}\left[\varphi_t, \kappa\right]$	$\operatorname{argth}({}^{0}\boldsymbol{t})$	$\arcsin({}^{\infty}\boldsymbol{t})$	$(B.2)$
$\varphi_t = \arcsin(\boldsymbol{t})$			
$\kappa = \left[\dfrac{\vartheta_2(q)}{\vartheta_3(q)}\right]^2$	$\tanh\left[\dfrac{\pi\Lambda_D}{4H} - \ln(2)\right]$	$4\, e^{-\pi H/\Lambda_D}$	
${}^{y}_{\theta}\!\vert\boldsymbol{t} = t_2 \cdot {}^{y}_{\theta}\!\vert\boldsymbol{w}$			$(B.3)$
${}_{x}\boldsymbol{t} = t_2 \cdot {}_{x}\boldsymbol{w} \Big/ \sqrt{1 + \left({}_{x}\boldsymbol{w}^2 - 1\right)\left(t_2 \cdot \kappa\right)^2}$			
t_2 : (see text)	$\tanh\left[\dfrac{\pi}{2}\dfrac{\frac{1}{2}\Lambda_c}{H}\right]$	$\sin\left[\pi\dfrac{\frac{1}{2}\Lambda_c}{\Lambda_D}\right]$	
$\boldsymbol{w} = \mathrm{sn}(\boldsymbol{s}, k)$	$\tanh({}^{y}_{\theta}\!\vert\boldsymbol{s})$	$\arcsin({}_{y}\boldsymbol{s})$	$(B.4)$
	$\sin({}_{x}\boldsymbol{s})$	$\mathrm{sn}({}^{\theta}_{x}\!\vert\boldsymbol{s}, {}^{\infty}_{x}\!\vert k)$	

Table B.1: Interdigital cut to parallel plates conformal mapping, $\boldsymbol{p} \leftarrow\!\shortmid\, \boldsymbol{s}$ backward sequences; $q = \exp(-2\pi H/\Lambda_D)$, see text for definitions of k *moduli*. F( ) incomplete elliptic integral of the first kind is written in trigonometric form. Reverting to $\boldsymbol{p} \mapsto \boldsymbol{s}$ sequence is straightforward, in particular: $\boldsymbol{s} = \mathrm{F}\left[\arcsin(\boldsymbol{w}), k\right]$, ${}_{x}\boldsymbol{w} = (\boldsymbol{t}/t_2)\sqrt{\left(1 - t_2^2\,\kappa^2\right)/\left(1 - \boldsymbol{t}^2\,\kappa^2\right)}$, and $\boldsymbol{t} = \mathrm{sn}\left(\boldsymbol{r}, \kappa\right)$.

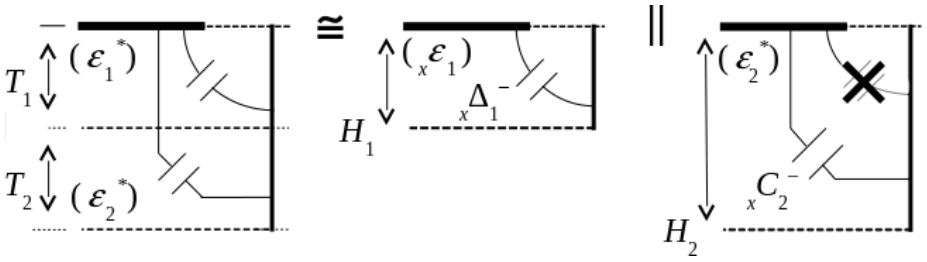

(a) Transverse PPC in coplanar scheme.

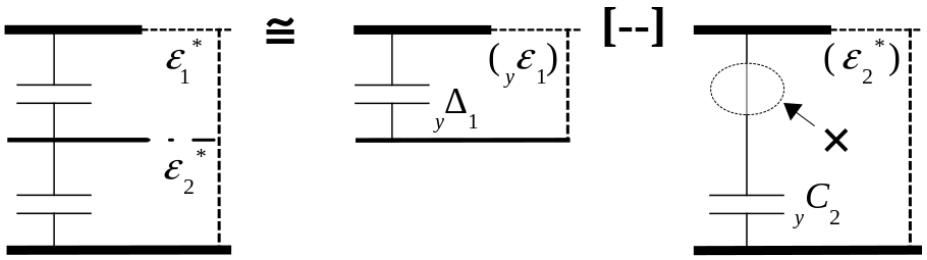

(b) Radial SPC on strip

Figure C.13: Ordinary partial capacitances (P.C.); close-up on left side of interdigital gap showing coplanar finger, strip backside, and capacitive parts. Symbols || and [- -] respectively identify parallel and series association of the latter [1]. Thick segments highlight equipotentials, dotted lines *isofluxes* for differential mode without back contact (a) or common mode on grounded backside (b). Note that $H_1 = T_1$ and $H_2 = T_1 + T_2$.

interfaces but through them – Dirichlet condition – such that SPC common-mode coupling results from mounting the partial admittances in series [48, 50, 52, 53]: ${}_yC = \left(1/{}_yC_2 + 1/{}_y\Delta_1\right)^{-1}$ (Fig. C.13-b). Variables Δ_n are defined in order to compensate for C_{n+1} overestimation in the extended layer:

$$
\begin{aligned}
{}_x\Delta_n^- &= {}_xC_n^- - \varepsilon_{n+1}^*\,{}_xCSR_n^- \;= {}_xCSR_n^-\left(\varepsilon_n^* - \varepsilon_{n+1}^*\right)\\
\frac{1}{{}_y\Delta_n} &= \frac{1}{{}_yC_n} - \frac{1}{\varepsilon_{n+1}^*\,{}_yCSR_n} = \frac{1}{{}_yCSR_n\left(\dfrac{1}{\varepsilon_n^*} - \dfrac{1}{\varepsilon_{n+1}^*}\right)^{-1}}.
\end{aligned}
$$

Terms between parenthesis are partial or per-layer "effective" permittivities. They may be used for implicit subtraction inside global sums compact formula, but rather when transverse and radial components do not combine.

References

[1] R. S. Pampin, Biocapteurs à réseaux d'électrodes isolées sur semiconducteur actif, Ph.D. thesis, UCL - SST/ICTM/ELEN - Pôle en ingénierie électrique (2012).
URL http://hdl.handle.net/2078.1/114724

[2] H. Ferhati, F. Djeffal, Performance assessment of Gr/Si/Gr UV-photodetector: Design and optimization of graphene interdigitated electrodes, Superlattices Microstruct. 132 (2019) 106166. doi:10.1016/j.spmi.2019.106166.

[3] X. Tang, et al., Direct protein detection with a nano-interdigitated array gate MOSFET, Biosens. Bioelectron. 24 (12) (2009) 3531 – 3537. doi:10.1016/j.bios.2009.05.012.

[4] E. F. Tsakas, A. N. Birbas, Noise associated with interdigitated gate structures in RF submicron MOSFETs, IEEE Trans. Electron Devices 47 (9) (2000) 1745–1750. doi:10.1109/16.861586.

[5] P. Hareesh, et al., Transverse interdigitated electrode actuation of homogeneous bulk PZT, J. Microelectromech. Syst. 21 (6) (2012) 1513–1518. doi:10.1109/JMEMS.2012.2211575.

[6] B. A. Cavic, M. Thompson, Interfacial nucleic acid chemistry studied by acoustic shear wave propagation, Anal. Chim. Acta 469 (1) (2002) 101 – 113. doi:10.1016/S0003-2670(01)01565-3.

[7] J. Green, et al., Novel programmable high-speed analog transversal filter, IEEE Electron Device Lett. 3 (10) (1982) 289–291. doi:10.1109/EDL.1982.25572.

[8] Y. Li, et al., A soft polydimethylsiloxane liquid metal interdigitated capacitor sensor and its integration in a flexible hybrid system for on-body respiratory sensing., Materials (12) (2019) 1458.

[9] C. Gaspar, et al., Paper as active layer in inkjet-printed capacitive humidity sensors, Sensors 17 (7) (2017) 1464. doi:10.3390/s17071464.

[10] C. Ataman, et al., A robust platform for textile integrated gas sensors, Sens. Actuators, B 177 (2013) 1053 – 1061. doi:10.1016/j.snb.2012.11.099.

[11] B. I. Morshed, et al., Investigation of low-voltage pulse parameters on electroporation and electrical lysis using a microfluidic device with interdigitated electrodes, IEEE Trans. Biomed. Eng. 61 (3) (2014) 871–882. doi:10.1109/TBME.2013.2291794.

[12] J. Do, et al., Low-cost magnetic interdigitated array on a plastic wafer, IEEE Trans. Magn. 40 (4) (2004) 3009–3011. doi:10.1109/TMAG.2004.828979.

[13] A. Ramos, et al., AC electric-field-induced fluid flow in microelectrodes, J. Colloid Interface Sci. 217 (2) (1999) 420 – 422. doi:10.1006/jcis.1999.6346.

[14] J. H. Chien, et al., Protein detection using a radio frequency biosensor with amplified gold nanoparticles, Appl. Phys. Lett. 91 (14) (2007) 143901. doi:10.1063/1.2794758.

[15] H. Baudrand, et al., Amplification by interdigital excitation of space-charge waves in semiconductors, IEEE Trans. Microw. Theory Tech. 32 (11) (1984) 1434–1441. doi:10.1109/TMTT.1984.1132868.

[16] G. S. Kino, F.E.T. theory of strip-coupled rayleigh-wave amplifier, Electron. Lett. 9 (3) (1973) 52–53. doi:10.1049/el:19730037.

[17] X. Bao, et al., Modeling of coplanar interdigital capacitor for microwave microfluidic application, IEEE Trans. Microw. Theory Tech. 67 (7) (2019) 2674–2683. doi:10.1109/TMTT.2019.2916871.

[18] T.-K. Chen, G. H. Huff, Analytical investigation of periodic coplanar waveguides, Prog. In Electromagn. Res. M 30 (2013) 167–181. doi:10.2528/PIERM13032110.

[19] Y. Wang, Superconducting coplanar delay lines, Ph.D. thesis, University of Birmingham (July 2005).

[20] C. H. Nguyen, et al., Probing-models for interdigitated electrode systems with ferroelectric thin films, J. Phys. D: Appl. Phys. 51 (17) (2018) 175303. doi:10.1088/1361-6463/aab2a1.

[21] M. N. Horenstein, et al., Differential capacitive position sensor for planar MEMS structures with vertical motion, Sens. Actuators, A 80 (1) (2000) 53 – 61. doi:10.1016/S0924-4247(99)00251-4.

[22] Y. Ren, et al., An electromagnetic/capacitive composite sensor for testing of thermal barrier coatings, Sensors (Basel, Switz.) 18 (5). doi:10.3390/s18051630.

[23] Y. Kim, et al., Development of lc resonator for label-free biomolecule detection, Sens. Actuators, A 143 (2) (2008) 279 – 285. doi:10.1016/j.sna.2007.11.014.

[24] Y. C. Lim, R. A. Moore, Properties of alternately charged coplanar parallel strips by conformal mappings, IEEE Trans. Electron Devices 15 (3) (1968) 173–180. doi:10.1109/T-ED.1968.16156.

[25] H. Wang, et al., Measurement of coating thickness and loading using concentric fringing electric field sensors, IEEE Sens. J. 14 (1) (2014) 68–78. doi:10.1109/JSEN.2013.2279991.

[26] C. Kim, et al., Numerical analysis on effective electric field penetration depth for interdigital impedance sensor, J. Phys. Conf. Ser. 418 (1) (2013) 012020. doi:10.1088/1742-6596/418/1/012020.

[27] R. Igreja, C. Dias, Dielectric response of interdigital chemocapacitors: The role of the sensitive layer thickness, Sens. Actuators, B 115 (1) (2006) 69 – 78. doi:10.1016/j.snb.2005.08.019.

[28] R. S. Pampin, et al., Bio-compatible insulated substrate impedance transducers, in: J. Vander Sloten, et al. (Eds.), 4th Eur. Conf. Int. Fed. Med. Biol. Eng. - ECIFMBE, Vol. 22, Springer Verlag, Antwerp, Belgium, 2009, pp. 221–238. doi:10.1007/978-3-540-89208-3_282.

[29] X. Tang, et al., A new interdigitated array microelectrode-oxide-silicon sensor with label-free, high sensitivity and specificity for fast bacteria detection, Sens. Actuators, B 156 (2) (2011) 578 – 587. doi:10.1016/j.snb.2011.02.002.

[30] L. Moreno-Hagelsieb, et al., Sensitive DNA electrical detection based on interdigitated Al/Al2O3 microelectrodes, Sens. Actuators, B 98 (2) (2004) 269 – 274. doi:10.1016/j.snb.2003.10.036.

[31] M. Vukadinovic, et al., Modelling and characterization of thin film planar capacitors: inherent errors and limits of applicability of partial capacitance methods, Meas. Sci. Technol. 20 (11) (2009) 115106. doi:10.1088/0957-0233/20/11/115106.

[32] N. Galopin, B. Delinchant, Coupled semianalytical and fem modeling of polymer piezoelectric material with interdigitated electrodes, IEEE Trans. Magn. 51 (3) (2015) 1–4. doi:10.1109/TMAG.2014.2365457.

[33] M. Cole, et al., Parametric model of a polymeric chemoresistor for use in smart sensor design and simulation, Microelectron. J. 34 (9) (2003) 865 – 875. doi:10.1016/S0026-2692(03)00131-9.

[34] A. Rivadeneyra, et al., Printed electrodes structures as capacitive humidity sensors: A comparison, Sens. Actuators, A 244 (2016) 56 – 65. doi:10.1016/j.sna.2016.03.023.

[35] A. E. Guennam, B. M. Luccioni, Model for piezoelectric/ferroelectric composites polarized with interdigitated electrodes, Compos. Struct. 131 (2015) 312 – 324. doi:10.1016/j.compstruct.2015.04.014.

[36] M. Mallén-Alberdi, et al., Impedance spectral fingerprint of E. coli cells on interdigitated electrodes: A new approach for label free and selective detection, Sens. Bio-Sens. Res. 7 (2016) 100 – 106. doi:10.1016/j.sbsr.2016.02.001.

[37] T. Voglhuber-Brunnmaier, et al., Semi-numeric model of capacitive touch sensors integrated into coatings of metallic substrates, in: IEEE SENSORS, 2017, pp. 1–3. doi:10.1109/ICSENS.2017.8233902.

[38] R. Liu, et al., Wall climbing robot using electrostatic adhesion force generated by flexible interdigital electrodes, Int. J. (Wash.) Adv. Robot. Syst. 10 (1) (2013) 36. doi:10.5772/54634.

[39] E. Glytsis, et al., Electric field, permittivity, and strain distributions induced by interdigitated electrodes on electrooptic waveguides, J. Lightwave Technol. 5 (5) (1987) 668–683. doi:10.1109/JLT.1987.1075558.

[40] B. N. H. Ymeri, K. Maex, Computation of conductance and capacitance for ic interconnects on a general lossy multilayer substrate, Act. Passive Electron. Compon. 24 (2) (2001) 87–114. doi:10.1155/2001/87589.

[41] N. G. Alexopoulos, C. M. Krowne, Characteristics of single and coupled microstrips on anisotropic substrates, IEEE Trans. Microw. Theory Tech. 26 (6) (1978) 387–393. doi:10.1109/TMTT.1978.1129399.

[42] M. L. Tounsi, M. C. E. Yagoub, Efficient design of wireless anisotropic circuits, in: 13th Int. Wirel. Commun. Mob. Comput. Conf. (IWCMC), 2017, pp. 866–869. doi:10.1109/IWCMC.2017.7986399.

[43] M. Horno, et al., Quasi-tem analysis of multilayered, multiconductor coplanar structures with dielectric and magnetic anisotropy including substrate losses, IEEE Trans. Microw. Theory Tech. 38 (8) (1990) 1059–1068. doi:10.1109/22.57331.

[44] S. I. Abramowitz M., Handbook Of Mathematical Functions with formulas, graphs, and mathematical tables, Vol. 55 of Applied Mathematics, Dover Publ. Inc., N. Y., 1972 / 1992.

[45] D. F. Lawden, Elliptic Functions and Applications, Vol. 80 of Applied Mathematical Science, Springer-Verlag, N. Y., 1989. doi:10.1007/978-1-4757-3980-0.

[46] S. S. Gevorgian, et al., CAD models for multilayered substrate interdigital capacitors, IEEE Trans. Microw. Theory Tech. 44 (6) (1996) 896–904. doi:10.1109/22.506449.

[47] J. Wei, Distributed capacitance of planar electrodes in optic and acoustic surface wave devices, IEEE J. Quantum Electron. 13 (4) (1977) 152–158. doi:10.1109/JQE.1977.1069319.

[48] S. O. Blume, et al., Modelling the capacitance of multi-layer conductor-facing interdigitated electrode structures, Sens. Actuators, B 213 (2015) 423 – 433. doi:10.1016/j.snb.2015.02.088.

[49] G. Ghione, M. Goano, Revisiting the partial-capacitance approach to the analysis of coplanar transmission lines on multilayered substrates, IEEE Trans. Microw. Theory Tech. 51 (9) (2003) 2007–2014. doi:10.1109/TMTT.2003.815873.

[50] R. Igreja, C. Dias, Extension to the analytical model of the interdigital electrodes capacitance for a multi-layered structure, Sens. Actuators, A 172 (2) (2011) 392 – 399. doi:10.1016/j.sna.2011.09.033.

[51] S. Gevorgian, et al., Basic parameters of coplanar-strip waveguides on multilayer dielectric/semiconductor substrates. part 2: Low permittivity superstrates, IEEE Microw. Mag. 4 (3) (2003) 59–78. doi:10.1109/MMW.2003.1237478.

[52] G. Ghione, et al., Microwave modeling and characterization of thick coplanar waveguides on oxide-coated lithium niobate substrates for electrooptical applications, IEEE Trans. Microw. Theory Tech. 47 (12) (1999) 2287–2293. doi:10.1109/22.808972.

[53] A. N. Sytchev, A model of the shielded multiconductor microstrip lines on double-layer substrate - a novel approach, in: Microw. Electron.: Meas., Identif., Appl. Conf., 2001. MEMIA 2001, 2001, pp. 77–81. doi:10.1109/MEMIA.2001.982325.

[54] C. Dias, R. Igreja, A method of recursive images to obtain the potential, the electric field and capacitance in multi-layer interdigitated electrode (IDE) sensors, Sens. Actuators, A 256 (2017) 95 – 106. doi:10.1016/j.sna.2017.01.021.

[55] O. G. Vendik, et al., Modeling and calculation of the capacitance of a planar capacitor containing a ferroelectric thin film, Tech. Phys. 44 (4) (1999) 349–355. doi:10.1134/1.1259300.

[56] E. Hammerstad, O. Jensen, in: IEEE MTT-S Int. Microw. Symp. Dig.

[57] C. Greebe, et al., Electric coupling properties of acoustic and electric surface waves, Phys. Rep. 1 (5) (1971) 235 – 268. doi:10.1016/0370-1573(71)90004-4.

[58] N. Pesonen, et al., Application of conformal mapping approximation techniques: parallel conductors of finite dimensions, IEEE Trans. Instrum. Meas. 53 (3) (2004) 812–821. doi:10.1109/TIM.2004.827065.

[59] N. Dib, Comprehensive study of CAD models of several coplanar waveguide (CPW) discontinuities, in: IEE Proc. Microw. Antennas Propag., Vol. 152, 2005, pp. 69–76. doi:10.1049/ip-map:20045039.

[60] N. Couniot, et al., Capacitive biosensing of bacterial cells: Analytical model and numerical simulations, Sens. Actuators, B 211 (2015) 428 – 438. doi:10.1016/j.snb.2015.01.108.

[61] W. Heinrich, Quasi-tem description of mmic coplanar lines including conductor-loss effects, IEEE Trans. Microw. Theory Tech. 41 (1) (1993) 45–52. doi:10.1109/22.210228.

[62] H. A. Wheeler, Transmission-line properties of a strip on a dielectric sheet on a plane, IEEE Trans. Microw. Theory Tech. 25 (8) (1977) 631–647. doi:10.1109/TMTT.1977.1129179.

[63] A. Haidar, et al., Investigating half precision arithmetic to accelerate dense linear system solvers, in: Proc. of the 8th Workshop on Latest Adv. in Scalable Algorithms for Large-Scale Syst., ScalA '17, ACM, N. Y., 2017, pp. 10:1–10:8. doi:10.1145/3148226.3148237.

[64] K. Ścibisz-Mordelska, R. Nielek, Lower precision calculation for option pricing, Comput. Sci. 18 (4).

[65] N. Dib, et al., CAD modeling of coplanar waveguide interdigital capacitor, Int. J. (Wash.) RF Microw. Comput.-Aided Eng. 15 (6) (2005) 551–559. doi:10.1002/mmce.20099.

[66] G. Niebling, A. Schlachter, Qualitative and quantitative gas analysis with non-linear interdigital sensor arrays and artificial neural networks, Sens. Actuators, B 27 (1) (1995) 289 – 292, eurosensors VIII. doi:10.1016/0925-4005(94)01603-F.

[67] R. Igreja, C. Dias, Analytical evaluation of the interdigital electrodes capacitance for a multi-layered structure, Sens. Actuators, A 112 (2) (2004) 291 – 301. doi:10.1016/j.sna.2004.01.040.

[68] W. Luther, W. Otten, Reliable computation of elliptic functions, J. UCS 4 (1) (1998) 25–33. doi:10.3217/jucs-004-01-0025.

[69] S. Eidelloth, R. Brendel, Analytical theory for extracting specific contact resistances of thick samples from the transmission line method, IEEE Electron Device Lett. 35 (1) (2014) 9–11. doi:10.1109/LED.2013.2290602.

[70] E. F. Chor, J. Lerdworatawee, Quasi-two-dimensional transmission line model (QTD-TLM) for planar ohmic contact studies, IEEE Trans. Electron Devices 49 (1) (2002) 105–111. doi:10.1109/16.974756.

[71] M. Ibrahim, et al., Geometric parameters optimization of planar interdigitated electrodes for bioimpedance spectroscopy, J. Electr. Bioimpedance 4 (1). doi:10.5617/jeb.304.

[72] K. Beilenhoff, et al., Open and short circuits in coplanar MMIC's, IEEE Trans. Microw. Theory Tech. 41 (9) (1993) 1534–1537. doi:10.1109/22.245673.

[73] K. Binns, P. Lawrenson, Analysis and Computation of Electric and Magnetic Field Problems, Pergamon Press book, 1963.

[74] R. Crampagne, et al., A simple method for determining the Green's function for a large class of mic lines having multilayered dielectric structures, IEEE Trans. Microw. Theory Tech. 26 (2) (1978) 82–87. doi:10.1109/TMTT.1978.1129317.

[75] R. Ivanic, et al., Thin film interdigitated electrode arrays applicable for non-invasive monitoring of human skin, in: ASDAM 2000. Conf. Proc. Third Int. EuroConf. Adv. Semicond. Devices Microsyst. (Cat. No.00EX386), 2000, pp. 319–322. doi:10.1109/ASDAM.2000.889510.

[76] L. Moreno-Hagelsieb, et al., Electrical detection of DNA hybridization: Three extraction techniques based on interdigitated Al/Al2O3 capacitors, Biosens. Bioelectron. 22 (910) (2007) 2199 – 2207. doi:10.1016/j.bios.2006.10.024.

[77] B. Foultier, Comparison of dna detection methods using nanoparticles and silver enhancement, IEE Proc. Nanobiotechnol. 152 (2005) 3–12(9).

[78] K. Wang, et al., Inverse formula of coupled-striplines by synthetic asymptote, Microw. Opt. Technol. Lett. 49 (6) (2007) 1309–1312. doi:10.1002/mop.22446.

[79] G. K. Reeves, B. Harrison, An analytical model for alloyed ohmic contacts using a trilayer transmission line model, IEEE Trans. Electron Devices 42 (8) (1995) 1536–1547. doi:10.1109/16.398670.

[80] H. Berger, Models for contacts to planar devices, Solid-State Electron. 15 (2) (1972) 145 – 158. doi:10.1016/0038-1101(72)90048-2.

[81] T. Swanenburg, Negative conductance of an interdigital electrode structure on a semiconductor surface, IEEE Trans. Electron Devices 20 (7) (1973) 630–637. doi:10.1109/T-ED.1973.17714.

[82] A. N. Sychev, et al., Combining the partial-capacitance and the conformal mapping techniques for analysis of the multiconductor microstrip lines, in: 44th Eur. Microw. Conf., 2014, pp. 410–413. doi:10.1109/EuMC.2014.6986457.